第 50 卷 第 1 期/2023 年 1 月/中国激光 特邀论文

中国激光

宽带隙二维半导体 $TlGaS_2$ 紫外探测器

龙浩然[1,2]，高媛[3]，刘浩[1,2]，辛凯耀[1,2]，于雅俐[1,2]，杨珏晗[1,2*]，魏钟鸣[1,2**]

[1]中国科学院半导体研究所半导体超晶格国家重点实验室，北京 100083；

[2]中国科学院大学材料与光电研究中心，北京 100049；

[3]军委装备发展部，北京 100032

摘要 紫外光电探测器是继红外激光探测技术之后发展起来的一种新型探测技术。其中基于宽带隙的低维半导体材料的紫外光电探测器是当下的研究热点之一。为了实现对宽带隙二维材料体系的拓宽以及高性能紫外探测器的研制，研究了机械剥离的铊镓硫（$TlGaS_2$）纳米片的能带结构以及光谱性质，制作了基于 $TlGaS_2$ 纳米片的紫外光电探测器。结果显示，$TlGaS_2$ 纳米片在紫外乃至日盲紫外波段均具有较高的吸收。探测器响应波段与光学吸收结果一致，对 360 nm 的紫外信号具有最佳的探测性能。此外，探测器在响应范围内均表现出了很低的暗电流以及优异的光电响应速度。测试结果说明了 $TlGaS_2$ 二维材料在紫外光电器件领域具有一定的研究前景和潜在的应用价值。

关键词 探测器；光电探测器；紫外光；铊镓硫纳米片；快速响应

中图分类号 TN23 **文献标志码** A **DOI：** 10.3788/CJL221103

1 引 言

光电探测器是光电子技术的关键核心元器件之一，其主要是通过光电效应将外部光信号转换为电信号，从而实现对光信号的收集与分析，在光通信、遥感、医疗、电子制造、火灾预警等众多领域有着极其重要的作用[1-2]。紫外探测器是继红外和激光探测技术之后发展起来的新型探测技术，相较于红外探测器，紫外探测器不会受到环境热源的影响，从而具有更高的信噪比，在各行业都具有重要的应用价值和广阔的发展前景[3-7]，成为了光电探测器研究的热点。

自石墨烯问世以来[8]，二维材料因为具有表面无悬挂键、层间通过 van der Waals 力连接、在构筑异质结时无需考虑晶格失配等优点而受到了广泛的研究，尤其在微电子与光电子领域[1,9]。常见二维半导体材料包括过渡金属硫族化合物（TMDs）[2,10-11]、黑磷[12-15]、Ⅳ-Ⅵ族化合物（如 GeSe[16]和 SnS[17]）等，均在光电探测领域得到了广泛的研究。但由于大多数二维材料的带隙宽度小于 2 eV，制作得到的探测器响应范围集中在可见光与近红外波段，难以实现对紫外波段的有效探测。目前文献报道的具有紫外光电性能的宽带隙二维材料有 GeS_2[18]、BiOBr[5]、$GaPS_4$[4]、Bi_2O_3[19]等，相较其他波段的材料种类较少，且都存在有响应速度慢等缺点[6-7,20]，因此扩展基于二维材料的紫外探测体系并提高紫外探测性能成为了研究重点。

$TlGaS_2$ 属于Ⅲ-Ⅵ族三元化合物 $TlBX_2$（B=Ga，In；X=S，Se，Te），具有层状结构[21]。由于其特殊结构，$TlGaS_2$ 具有低温相变[22]和非线性光学效应[23]，其拉曼光谱、吸收光谱、光致发光光谱等得到了广泛的研究[24-28]。$TlGaS_2$ 具有 2.35～2.46 eV 的间接带隙和 2.38～2.64 eV 的直接带隙[28]，能够对紫外光实现有效的吸收，在光电器件领域具有应用潜力[29]。然而，目前鲜有工作报道基于 $TlGaS_2$ 纳米片的紫外探测器性能。

本文使用机械剥离的方法获取了 $TlGaS_2$ 纳米片，通过拉曼光谱以及 X 射线光电子能谱表征了纳米片，证明了其具有良好的晶体质量。理论计算了其能带结构，计算结果与实验测试得到的吸收光谱结果一致，在紫外至日盲紫外波段均具有较高的吸收。利用电子束曝光技术制作了两端探测器器件，通过一系列光电测试，发现基于 $TlGaS_2$ 纳米片的光电探测器能够实现对波长小于 400 nm 的紫外乃至日盲紫外信号的有效探测，表现出了很低的暗电流和极为优异的光响应速度，暗电流能够保持在 10^{-13} A 量级，开态和关态的响应时间分别达到了 51.8 μs 和 45.1 μs，优于大多数宽带隙二维材料紫外探测器。探测器在 360 nm 处具有最好的响应性能，开关比能够达到 10^4，响应度为 57 mA/W，比探测率为 2.69×10^{10} cm·$Hz^{1/2}$·W^{-1}，同时器件具有良好的空气稳定性。我们还利用光电流二维平

收稿日期：2022-08-03；**修回日期**：2022-09-01；**录用日期**：2022-09-07；**网络首发日期**：2022-09-17

基金项目：国家自然科学基金（62004193）

通信作者：*yjhyjg@semi.ac.cn；**zmwei@semi.ac.cn

面扫描(mapping)测试揭示了 $TlGaS_2$ 探测器的工作原理。

2 实验方法

2.1 器件制作方法

实验中探测器制作采用了 $TlGaS_2$ 单晶。利用胶带将 $TlGaS_2$ 单晶进行机械剥离，通过聚二甲基硅氧烷(PDMS)将胶带上剥离得到的纳米片转移到 SiO_2/Si 衬底上。在有纳米片的衬底上旋涂一层电子束胶，用电子束曝光技术(EBL)对其进行图案化处理，再用电子束蒸发技术沉积 20 nm/50 nm 厚度的 Ti/Au 以作为探测器两端电极，最后使用丙酮进行剥离以留下电极的部分。

2.2 材料表征及器件测试

材料结构及化学组分表征使用了拉曼光谱(激发波长为 532 nm)和 X 射线光电子能谱(XPS)。材料厚度通过原子力显微镜(AFM)测量。材料吸收光谱由显微分光光度计测试得到，光谱测试范围为 250～1000 nm。器件电学及光电性质均通过半导体器件分析测试仪得到，光电测试光源为 360 nm 和 405 nm 激光器，其余波长光通过在汞灯出光口处放置相应波长的滤光片得到。

2.3 理论计算方法

基于密度泛函理论，采用 VASP 软件包[30]进行了第一性原理的相关计算，得到了材料的能带结构和态密度。其中，由投影缀加平面波(PAW)方法[31]得到的赝势描述离子实与价电子的相互作用。由于基于 PBE(Perdew-Burke-Ernzerhof)泛函的计算会低估带隙，因此本文采用了杂化泛函[32]，其中杂化泛函的库仑屏蔽因子为 0.15，组合系数为 0.3。平面波展开的截断能为 400 eV，能量收敛到 10^{-5} eV。在布里渊区积分过程中，采用 Monkhorst-Pack 方法产生了 4×4×3 的 k 点网格并进行取样。

3 分析与讨论

图 1(a)为 $TlGaS_2$ 的晶体结构示意图，其结构空间群为 C2/c，属于单斜晶系，c 轴与 ab 平面间的夹角约为 100°，单胞的点阵参数分别为 $a=b=1.04$ nm，$c=1.517$ nm[33]。其晶格单层由平行于(001)平面的金属原子和硫原子交替组成，晶体单胞由两层 $TlGaS_2$ 构成，每一层相较前一层旋转了 90°。层间通过 van der Waals 力连接，层内为作用力很强的共价键，因此可以通过胶带延 c 轴方向进行机械剥离。机械剥离后的 $TlGaS_2$ 纳米片被 PDMS 转移到 SiO_2/Si 衬底上以进行进一步的器件制作，图 1(b)为衬底上纳米片的光学显微镜照片。机械剥离得到的 $TlGaS_2$ 纳米片厚度通常为 50～300 nm，难以得到薄层，这可能是由于其层间的 van der Waals 力比石墨烯、二硫化钼等其他二维材料较强[34]。由于纳米片的厚度较大，利用此纳米片制作的横向探测器性能与纳米片的厚度之间没有必然联

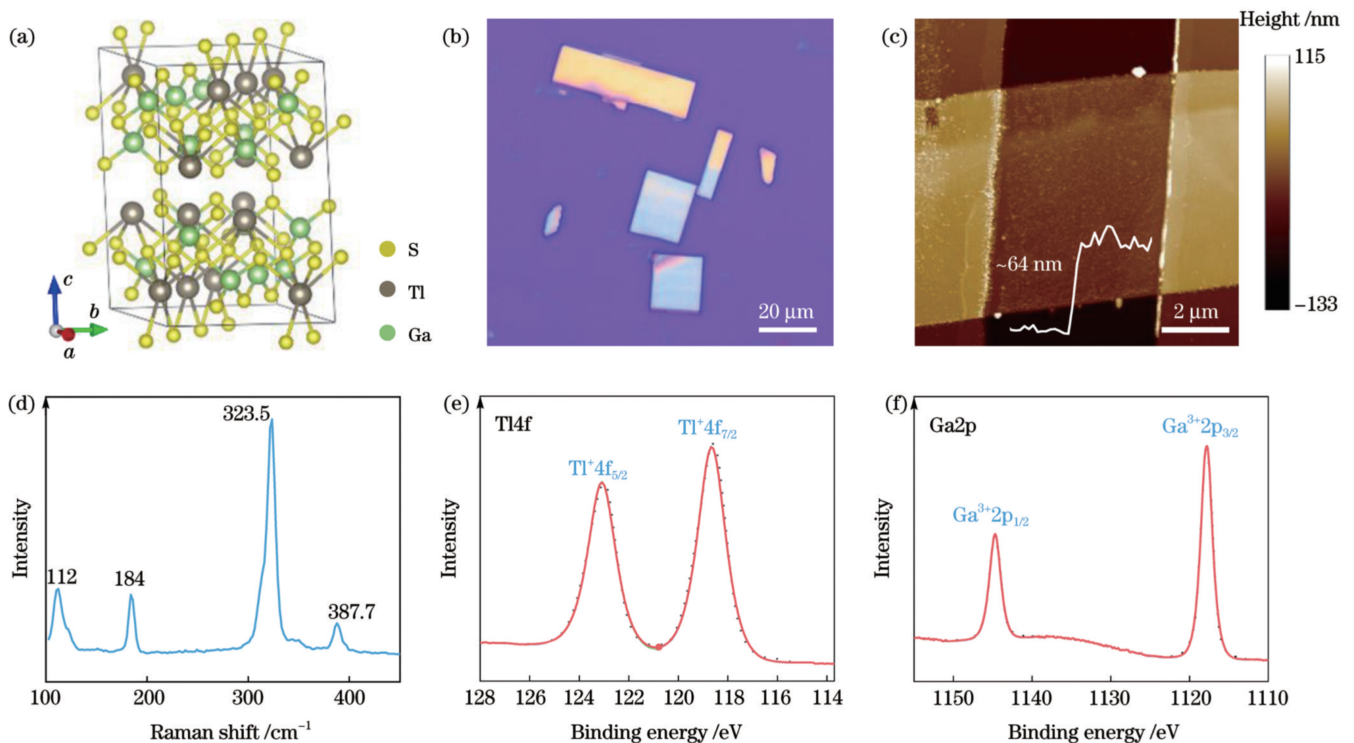

图 1 晶体结构及材料表征结果。(a) $TlGaS_2$ 晶体结构图；(b)纳米片光学显微镜照片；(c)原子力显微镜测试；(d)拉曼测试结果；(e)元素 Tl 和(f)元素 Ga 的 X 射线光电子能谱测试结果

Fig. 1 Crystal structure and material characterization results. (a) $TlGaS_2$ crystal structure; (b) optical microscope photos of nanosheets; (c) AFM test; (d) Raman test result; XPS test results of elements (e) Tl and (f) Ga

系。后文所报道的探测器性能均基于 64 nm 的 $TlGaS_2$ 纳米片，AFM 测试如图 1(c)所示。

利用显微拉曼光谱技术，对剥离的纳米片进行了表征，如图 1(d)所示。测试范围为 100～500 cm^{-1}，测试结果显示在测试范围内有 4 个振动峰，分别位于 112.0、184.0、323.5、387.7 cm^{-1}，峰位与文献[23]报道几乎一致。图 1(e)、(f)为 $TlGaS_2$ 材料的 X 射线光电子能谱的测试结果。结果显示，Tl 元素的结合能分别为 123 eV 和 118.5 eV，对应 $Tl^{+}4f_{5/2}$ 和 $Tl^{+}4f_{7/2}$，说明了 Tl 元素在化合物中以+1 价的形式参与成键；Ga 原子的结合能位于 1144.7 eV 和 1117.8 eV，分别对应 $Ga^{3+}2p_{1/2}$ 和 $Ga^{3+}2p_{3/2}$，说明了化合物中 Ga 元素的价态为+3 价[35]。

图 2(a)为 $TlGaS_2$ 体材料的能带计算结果，理论计算结果显示 $TlGaS_2$ 为间接带隙半导体，价带顶位于 Γ 点，禁带宽度为 2.59 eV，同时其在 Γ 点处具有 2.76 eV 的直接带隙，与文献[21,24,28]报道的结果几乎一致。态密度[图 2(b)]结果显示，$TlGaS_2$ 材料的价带顶的电子态密度主要由 S 原子贡献，而导带底主要由 Tl 原子贡献。图 2(c)为 $TlGaS_2$ 纳米片的吸收光谱测试结果，其中在小于 3 eV 的波长范围内，由于纳米片的厚度较大，在吸收光谱的测试过程中出现了干涉效应，从而曲线出现了一些微小的起伏。从 2.6 eV (480 nm)处开始，材料吸收率逐渐增加，正好对应其在 2.59 eV 处的间接带隙特征。材料在 2.85 eV (430 nm)附近出现了一个陡峭的吸收边，符合直接带隙跃迁的吸收谱特征，这一吸收边略大于材料理论计算得到的 2.76 eV 直接带隙，可能是计算误差导致的。结果说明了 $TlGaS_2$ 纳米片在 430 nm 波段出现了间接带隙跃迁向直接带隙跃迁的转变。$TlGaS_2$ 材料的能带特征使得其在紫外至深紫外均具有较高的吸收率，在紫外光电器件中具有潜在的应用前景。

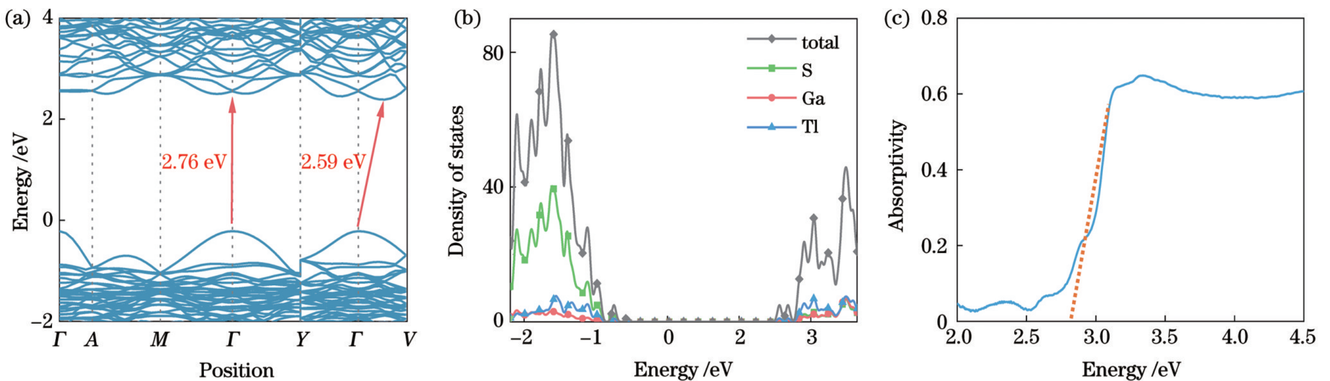

图 2 理论计算及吸收谱测试结果。(a) $TlGaS_2$ 体材料的能带结构；(b)带边处的态密度示意图；(c) $TlGaS_2$ 纳米片的吸收光谱测试结果

Fig. 2 Theoretical calculation and absorption spectrum test results. (a) Energy band structure of $TlGaS_2$ bulk material; (b) density of states at band edge; (c) measured absorption spectrum of $TlGaS_2$ nanosheet

通过电子束曝光及蒸发沉积金属后得到了 $TlGaS_2$ 光电探测器的器件结构，如图 3(a)所示。图 3(b)为器件在暗态和紫外光激发下的电流-电压输出曲线，器件两端施加了−5～+5 V 的输入电压，各波长光信号的功率密度均为 100 mW/cm^2，其中插图为实际用于测试的 $TlGaS_2$ 光电探测器的光学显微镜照片。测试结果显示，由于 $TlGaS_2$ 具有较宽的带隙特征，探测器对紫外光信号均表现出了明显的光电响应特征，尤其对 280 nm 的日盲紫外信号同样具有明显的光电响应。同时暗态下载流子浓度较低，探测器暗电流维持在 10^{-13} A 量级，如此低的暗电流有利于探测器对光信号的探测。此外，无论是在暗态还是在紫外光探测模式下，输出曲线均保持着较好的近线性特征，暗示了材料与 Ti/Au 电极之间的接触形式为欧姆接触。为了探索探测器的响应波长范围，在相同功率密度(20 mW/cm^2)下，利用不同波长的光源进行了测试，测试范围为 300～600 nm，步长为 10 nm，测试两端施加的电压为 5 V，测试结果如图 3(c)所示。$TlGaS_2$ 光电探测器对波长小于 480 nm 的信号均具有一定的响应，响应趋势与材料吸收谱的变化一致，从 430 nm 附近开始陡峭增加，对 360 nm 附近的紫外信号具有最大的光响应电流。为了表征探测器性能，对其响应度及比探测率进行了计算。

$$R=\frac{I_{ph}}{PA}, \tag{1}$$

$$D^{*}=\frac{R\sqrt{A}}{\sqrt{2eI_{dark}P}}, \tag{2}$$

式中：R 为探测器响应度，通常反映了探测器的输入-输出增益，单位为 A/W 或 mA/W；D^{*} 为比探测率，反映了探测器能够检测到的最小功率，表征了器件性能的品质因数；P 为入射光功率密度；A 为探测器的光吸收面积；I_{ph} 和 I_{dark} 分别为探测器在光照和暗态下的输出电流；e 为单位电荷量。计算结果如图 3(d)所示，在 360 nm 紫外波长下具有最优的探测性能，响应度为 57 mA/W，比探测率为 2.69×10^{10} $cm\cdot Hz^{1/2}\cdot W^{-1}$。进一步研究了探测器在不同光照功率密度下的瞬态响应特征，测试波长为 360 nm，两端电压为 5 V[图 3(e)]。结果表明：该器件具有稳定的瞬态响应性能，暗电流能

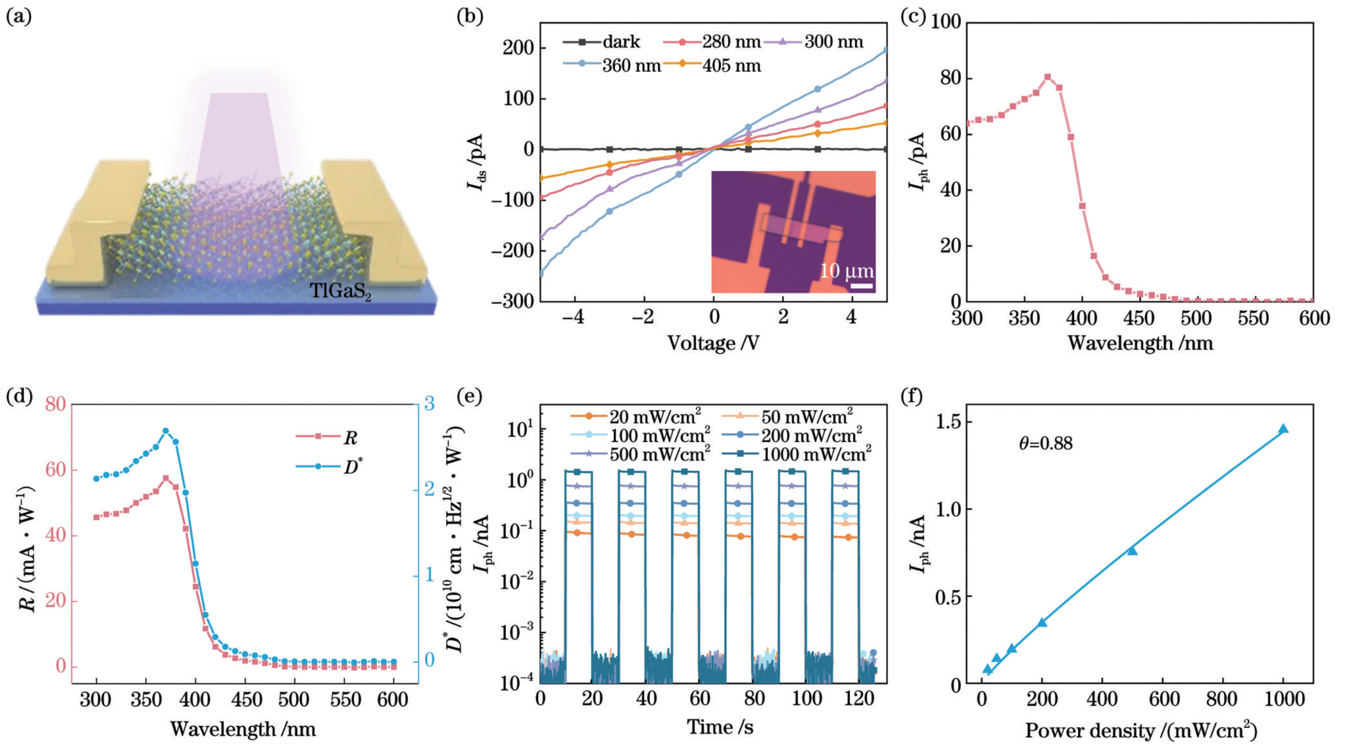

图 3　$TlGaS_2$光电探测器的光电性能测试结果。(a)$TlGaS_2$探测器的结构示意图;(b)暗态及不同波长光照射条件下的输出曲线(插图为器件的光学显微镜照片);(c)探测器的光谱响应范围;(d)响应度和比探测率随波长的变化;(e)在 360 nm 处不同光功率密度下的瞬态响应测试结果;(f)光电流与光功率密度的关系

Fig. 3　Test results of photoelectric performances of $TlGaS_2$ photodetector. (a) Structural diagram of $TlGaS_2$ detector; (b) output curves under dark state and different wavelength light irradiation conditions with optical microscope photo of device shown in insert; (c) spectral response range of detector; (d) responsivity and specific detection rate versus wavelength; (e) transient response test results under different optical power densities at 360 nm; (f) photocurrent versus optical power density

够保持在 10^{-13} A 量级,在 1 W/cm^{2}的入射光照射下开关比达到了 10^4;对于更小的激光强度照射,器件开关比基本维持在 10^3,且随着入射光的开和关,陡峭的上升沿和下降沿表明探测器具有较快的响应速度,说明纳米片产生的光生载流子能够在器件中迅速分离并被电极收集[36]。提取了不同功率密度下的光电流数值并进行了拟合:

$$I_{ph}=\alpha P^{\theta},\tag{3}$$

式中:α 为比例常数;θ 为经验常数。在一定程度上式(3)能够反映器件对光的利用率和响应能力,θ 越趋近于 1 表明器件对光的利用率越高,光电导效应占主导作用。拟合结果如图 3(f)所示,θ 为 0.88,接近于 1,表明该探测器主要是通过光电导效应实现了光信号向电信号的转变。

由瞬态光电测试结果可知,$TlGaS_2$光电探测器表现出了优秀的响应速度,通过高速开关(开关频率为 1 kHz)与锁相放大器准确测量了其响应时间。图 4(a)所示的测试结果显示,在 360 nm 紫外光探测下 $TlGaS_2$ 光电探测器的开态与关态时间分别达到了 51.8 μs 和 45.1 μs,在有文献报道的宽禁带二维材料光电探测器中较有优势,详细的性能对比如表 1 所示。如此快速的响应除了与材料本身的光载流子动力学性质有关,还可能是由于材料的高晶体质量以及其与金属电极之间形成的良好欧姆接触,因此光生载流子能够在外场的作用下快速分离。图 4(b)是探测器在弱光环境下的频率依赖的噪声测试结果,其中 S 为噪声功率谱密度。测试结果显示,器件在 1 Hz 频率下具有较低的噪声电流,约为 0.7 pA。根据 Hooge 公式,对曲线进行拟合:

$$S=S_0\frac{I^b}{f^a},\tag{4}$$

式中:S_0 为 Hooge 参数;I 为流经探测器的电流;f 为测试频率;a 和 b 均为拟合得到的常数。拟合得到的常数 a 为 0.95,非常接近于 1,说明 $TlGaS_2$器件在低频下主要为 $1/f$ 噪声,这是由载流子在输运过程中的涨落导致的。如此低的噪声也暗示了其在紫外探测成像方面具有潜在应用。同时 $TlGaS_2$光电探测器还表现出了不错的空气稳定性,器件在三个月的瞬态响应测试中的性能开关比仅发生了 3% 的衰减,开关速度几乎没有发生变化。

图 4(d)为 $TlGaS_2$光电探测器的光电流 mapping 测试图,测试所使用的光源为 0.1 μW 的 405 nm 激光,器件两端电压为 5 V,mapping 测试步长为 0.3 μm,测试图中水平虚线之间的区域为材料所在位置,两个竖

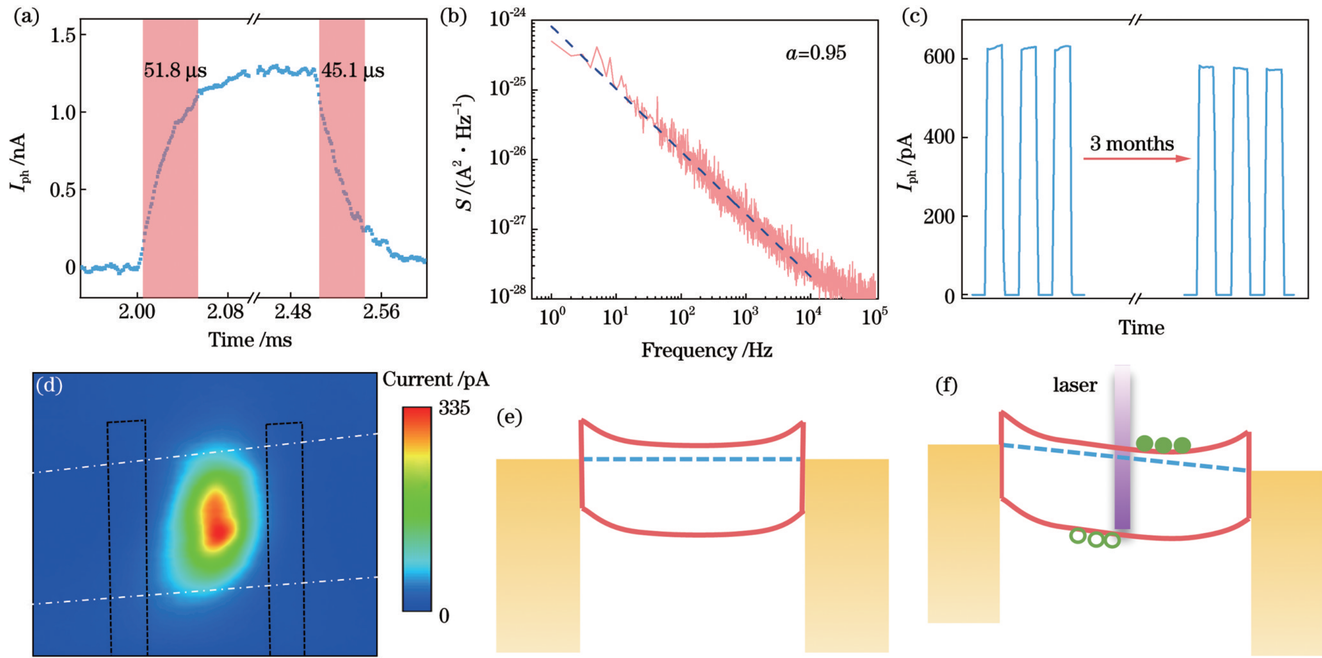

图 4　$TlGaS_2$光电探测器的工作性能与工作原理。(a)响应速度;(b)弱场下的噪声性能;(c)空气稳定性;(d)光电流二维平面扫描测试;(e)(f)探测器工作原理

Fig. 4　Working performances and principle of $TlGaS_2$ photodetector. (a) Response speed; (b) noise performance under weak field; (c) air stability; (d) photocurrent two-dimensional plane scanning test; (e)(f) working principle of detector

表 1　基于宽禁带材料的紫外光电探测器的性能对比

Table 1　Performance comparison of ultraviolet photodetectors based on wide bandgap materials

Material	Wavelength /nm	Responsivity /(mA·W^{-1})	Response time (rise/delay)	Reference
$CuGaS_2$	254	5.1×10^3	1.8 s/10.1 s	[37]
PbI_2	375	510	14.1 ms/31.0 ms	[38]
$FePS_3$	254	170	105 ms/120 ms	[39]
$GaPS_4$	254	791	~50 ms	[4]
BiOBr	315	1.2×10^7	110 μs/160 μs	[5]
Bi_2O_3	300	2.21×10^3	290 μs/870 μs	[19]
$GeSe_2$	355	127	<30 ms	[40]
h-BN	212	0.1	320 ms/630 ms	[20]
GaN	360	251	1.12 ms/2.80 ms	[41]
Ga_2O_3	254	39.3	84.83 s/219.19 s	[42]
ZnO	370	10.5	1.4 s/6.8 s	[43]
$TlGaS_2$	360	57	51.8 μs/45.1 μs	This work

直虚线框为电极所在位置。由 mapping 测试图可见，探测器光电流的产生发生在材料内部，说明了该探测器在两端电极处具有良好的欧姆接触。探测器的工作原理由图 4(e)、(f)给出：材料与 Ti/Au 电极接触后，费米能级处于同一平面上，在界面处形成了势垒很小的欧姆接触。$TlGaS_2$材料在受到紫外光辐照后，材料内部由于紫外光的激发，电子跃迁到导带上形成光载流子。当电极两端加上外场，受到两端电势差的影响，导带中的光生电子和价带中的光生空穴加速分离并分别向电极两端移动形成光电流，从而实现了光信号向电信号的转换。

4　结　　论

研究了机械剥离的$TlGaS_2$纳米片的晶体结构和化学组分，发现了 Tl、Ga 元素在化合物中分别以+1 价与+3 价的形式存在。通过密度泛函理论计算了$TlGaS_2$的能带结构与态密度，计算得到的带隙值与吸收光谱实验测量得到的光学带隙值几乎一致；同时吸收谱测试结果表明，$TlGaS_2$材料在紫外至日盲紫外均具有较高的吸收，并且在 440 nm 处出现间接带隙跃迁

向直接带隙跃迁的转变。成功制作了基于 $TlGaS_2$ 纳米片的光电探测器,其工作原理为两端欧姆接触下的光电导效应产生的光生载流子在外场作用下形成光电流。探测器的工作波长范围与吸收谱一致,均小于 480 nm,尤其对波长小于 400 nm 的紫外乃至日盲紫外信号均能够实现有效的探测。探测器对 360 nm 信号具有最佳的响应度与探测率,同时表现出了很低的暗电流($\sim10^{-13}$ A)和极快的响应时间(开态 51.8 μs,关态 45.1 μs),优于大多数宽禁带二维材料光电探测器。这一工作为研究高响应速度的二维材料紫外光电探测器或抑制探测器的暗电流提供了新的材料选择。

参 考 文 献

[1] Bonaccorso F, Sun Z, Hasan T, et al. Graphene photonics and optoelectronics[J]. Nature Photonics, 2010, 4(9): 611-622.

[2] Tan P H, Zhang L J, Dai L, et al. Preface to the special issue on 2D-materials-related physical properties and optoelectronic devices [J]. Journal of Semiconductors, 2019, 40(6): 060101.

[3] Soci C, Zhang A, Xiang B, et al. ZnO nanowire UV photodetectors with high internal gain[J]. Nano Letters, 2007, 7 (4): 1003-1009.

[4] Yan Y, Yang J H, Du J, et al. Cross-substitution promoted ultrawide bandgap up to 4.5 eV in a 2D semiconductor: gallium thiophosphate[J]. Advanced Materials 2021, 33(22): 2008761.

[5] Gong C H, Chu J W, Qian S F, et al. Large-scale ultrathin 2D wide-bandgap BiOBr nanoflakes for gate-controlled deep-ultraviolet phototransistors[J]. Advanced Materials, 2020, 32(12): 1908242.

[6] Yang W, Xin K Y, Yang J H, et al. 2D ultrawide bandgap semiconductors: odyssey and challenges[J]. Small Methods, 2022, 6(4): 2101348.

[7] 王江, 罗林保. 基于氧化镓日盲紫外光电探测器的研究进展[J]. 中国激光, 2021, 48(11): 1100001.
Wang J, Luo L B. Advances in Ga_2O_3-based solar-blind ultraviolet photodetectors[J]. Chinese Journal of Lasers, 2021, 48(11): 1100001.

[8] Novoselov K S, Geim A K, Morozov S V, et al. Electric field effect in atomically thin carbon films[J]. Science, 2004, 306(5696): 666-669.

[9] Zhu W K, Wei X, Yan F G, et al. Broadband polarized photodetector based on p-BP/n-ReS_2 heterojunction[J]. Journal of Semiconductors, 2019, 40(9): 092001.

[10] Huang C, Jin Y B, Wang W Y, et al. Manganese and chromium doping in atomically thin MoS_2[J]. Journal of Semiconductors, 2017, 38(3): 033004.

[11] Wang Q H, Kalantar-Zadeh K, Kis A, et al. Electronics and optoelectronics of two-dimensional transition metal dichalcogenides [J]. Nature Nanotechnology, 2012, 7(11): 699-712.

[12] Deng N Q, Tian H, Zhang J, et al. Black phosphorus junctions and their electrical and optoelectronic applications[J]. Journal of Semiconductors, 2021, 42(8): 081001.

[13] Guo Q S, Pospischil A, Bhuiyan M, et al. Black phosphorus mid-infrared photodetectors with high gain[J]. Nano Letters, 2016, 16 (7): 4648-4655.

[14] Wang Y H, Sun S, Zhang J L, et al. Recent progress in epitaxial growth of two-dimensional phosphorus[J]. SmartMat, 2021, 2(3): 286-298.

[15] 任智慧, 钟绵增, 杨珏晗, 等. 基于 AsP/MoS_2 异质结的偏振光电探测器[J]. 中国光学, 2021, 14(1): 135-144.
Ren Z H, Zhong M Z, Yang J H, et al. A polarization-sensitive photodetector based on a AsP/MoS_2 heterojunction[J]. Chinese Optics, 2021, 14(1): 135-144.

[16] Wang X T, Li Y T, Huang L, et al. Short-wave near-infrared linear dichroism of two-dimensional germanium selenide[J]. Journal of the American Chemical Society, 2017, 139(42): 14976-14982.

[17] Zhou X, Gan L, Zhang Q, et al. High performance near-infrared photodetectors based on ultrathin SnS nanobelts grown via physical vapor deposition[J]. Journal of Materials Chemistry C, 2016, 4 (11): 2111-2116.

[18] Yusi Y, Liu S C, Wang X, et al. Polarization-sensitive ultraviolet photodetection of anisotropic 2D GeS_2[J]. Advanced Functional Materials, 2019, 29(16): 1900411.

[19] Wu J, Wang F K, Li H B, et al. Epitaxial growth of 2D ultrathin metastable γ-Bi_2O_3 flakes for high performance ultraviolet photodetection[J]. Small, 2022, 18(3): 104244.

[20] Liu H, Meng J H, Zhang X W, et al. High-performance deep ultraviolet photodetectors based on few-layer hexagonal boron nitride[J]. Nanoscale, 2018, 10(12): 5559-5565.

[21] Delgado G E, Mora A J, Pérez F V, et al. Crystal structure of the ternary semiconductor compound thallium gallium sulfide, $TlGaS_2$ [J]. Physica B: Condensed Matter, 2007, 391(2): 385-388.

[22] Aydinli A, Ellialtioğlu R, Allakhverdiev K R, et al. Low-temperature phase transitions in $TlGaS_2$ layer crystals[J]. Solid State Communications, 1993, 88(5): 387-390.

[23] Xin X F, Liu F, Yan X Q, et al. Two-photon absorption and non-resonant electronic nonlinearities of layered semiconductor $TlGaS_2$ [J]. Optics Express, 2018, 26(26): 33895-33905.

[24] Isik M, Gasanly N M, Turan R. Spectroscopic ellipsometry study of above-band gap optical constants of layered structured $TlGaSe_2$, $TlGaS_2$ and $TlInS_2$ single crystals[J]. Physica B: Condensed Matter, 2012, 407(21): 4193-4197.

[25] Isik M, Gasanly N M, Korkmaz F. Multiphonon absorption processes in layered structured $TlGaS_2$, $TlInS_2$ and $TlGaSe_2$ single crystals[J]. Physica B: Condensed Matter, 2013, 421: 50-52.

[26] Gasanly N M, Aydinli A, Bek A, et al. Low-temperature photoluminescence spectra of layered semiconductor $TlGaS_2$[J]. Solid State Communications, 1998, 105(1): 21-24.

[27] Kawabata T, Shim Y, Wakita K, et al. Dielectric function spectra and inter-band optical transitions in $TlGaS_2$[J]. Thin Solid Films, 2014, 571: 589-592.

[28] Qasrawi A F, Gasanly N M. Optoelectronic and electrical properties of $TlGaS_2$ single crystal[J]. Physica Status Solidi (a), 2005, 202(13): 2501-2507.

[29] Fu Y, He D W, He J Q, et al. Photocarrier dynamics in $TlGaS_2$ nanoflakes and van der Waals heterostructures with hexagonal boron nitride and WS_2 nanoflakes: implications for optoelectronic applications[J]. ACS Applied Nano Materials, 2020, 3(9): 8702-8707.

[30] Kresse G, Furthmüller J. Efficient iterative schemes for *ab initio* total-energy calculations using a plane-wave basis set[J]. Physical Review B, 1996, 54(16): 11169-11186.

[31] Blöchl P E. Projector augmented-wave method[J]. Physical Review B, 1994, 50(24): 17953-17979.

[32] Heyd J, Scuseria G E, Ernzerhof M. Hybrid functionals based on a screened Coulomb potential[J]. The Journal of Chemical Physics, 2003, 118(18): 8207-8215.

[33] Ashraf I M. Photophysical properties of $TlGaS_2$ layered single crystals[J]. The Journal of Physical Chemistry B, 2004, 108(30): 10765-10769.

[34] Tang K W, Qi W H, Wei Y R, et al. High-throughput calculation of interlayer van der Waals forces validated with experimental measurements[J]. Research, 2022, 2022: 9765121.

[35] Major G H, Fairley N, Sherwood P M A, et al. Practical guide for curve fitting in X-ray photoelectron spectroscopy[J]. Journal of Vacuum Science & Technology A: Vacuum, Surfaces, and Films, 2020, 38(6): 061203.

[36] 林亚楠, 吴亚东, 程海洋, 等. $PdSe_2$ 纳米线薄膜/Si 异质结近红外集成光电探测器[J]. 光学学报, 2021, 41(21): 2125001.
Lin Y N, Wu Y D, Cheng H Y, et al. Near-infrared integrated

photodetector based on $PdSe_2$ nanowires film/Si heterojunction[J]. Acta Optica Sinica, 2021, 41(21): 2125001.

[37] Xin B, Wu Y T, Liu X R, et al. High performance UV photodetector based on 2D non-layered $CuGaS_2$ nanosheets[J]. Semiconductor Science and Technology, 2019, 34(5): 055007.

[38] Xiao H, Liang T, Xu M S. Growth of ultraflat PbI_2 nanoflakes by solvent evaporation suppression for high-performance UV photodetectors[J]. Small, 2019, 15(33): 1901767.

[39] Gao Y, Lei S J, Kang T T, et al. Bias-switchable negative and positive photoconductivity in 2D $FePS_3$ ultraviolet photodetectors [J]. Nanotechnology, 2018, 29(24): 244001.

[40] Yan Y, Xiong W Q, Li S S, et al. Direct wide bandgap 2D $GeSe_2$ monolayer toward anisotropic UV photodetection[J]. Advanced Optical Materials, 2019, 7(19): 1900622.

[41] Wu G H, Du L Y, Deng C C, et al. High-performance self-driven single GaN-based p-i-n homojunction one-dimensional microwire ultraviolet photodetectors[J]. ACS Applied Electronic Materials, 2022, 4(8): 3807-3814.

[42] Kong W Y, Wu G A, Wang K Y, et al. Graphene-β-Ga_2O_3 heterojunction for highly sensitive deep UV photodetector application[J]. Advanced Materials, 2016, 28(48): 10725-10731.

[43] 孙立奇，王登魁，房丹，等. CdSe量子点修饰ZnO微米线快速响应的紫外光电探测器[J]. 中国激光，2022，49(13): 1303001.
Sun L Q, Wang D K, Fang D, et al. Quantum dots modified ZnO based fast-speed response ultraviolet photodetector[J]. Chinese Journal of Lasers, 2022, 49(13): 1303001.

Ultraviolet Photodetector Based on Wide Bandgap Two-Dimensional Semiconductor $TlGaS_2$

Long Haoran[1,2], Gao Yuan[3], Liu Hao[1,2], Xin Kaiyao[1,2], Yu Yali[1,2], Yan Juehan[1,2*], Wei Zhongming[1,2**]

[1] *State Key Laboratory of Superlattices and Microstructures, Institute of Semiconductors, Chinese Academy of Sciences, Beijing* 100083, *China*;

[2] *Center of Materials Science and Optoelectronics Engineering, University of Chinese Academy of Sciences, Beijing* 100049, *China*;

[3] *Center of Military Commission Equipment Development Department, Beijing* 100032, *China*

Abstract

Objective Ultraviolet (UV) detectors are a new detection technology developed after infrared and laser detection technologies. Compared with infrared detectors, UV detectors have a higher signal-to-noise ratio because they are not affected by environmental heat sources. Thus, UV detectors have potential value and development prospects in many fields, including optical communication, medical treatment, electronics, and fire warning. Two-dimensional materials have been widely studied in the field of photodetectors in recent years owing to the absence of dangling bonds on the surface, interlayers linked by van der Waals forces, and no lattice mismatch when constructing heterojunctions. However, research on UV photodetectors based on two-dimensional materials is faced with the problems of few wide-bandgap two-dimensional materials and poor detector performance, particularly slow response speed. This work reports the energy band structure and optical absorption characteristics of a novel wide-bandgap two-dimensional semiconductor, $TlGaS_2$. A UV photodetector based on a $TlGaS_2$ nanosheet is fabricated. The detector exhibits a clear response from the UV to solar-blind UV spectral regions, lower dark currents, and faster response speeds. We hope that our research can broaden the wide-bandgap two-dimensional material system, and provide new ideas and methods for the realization of high-performance two-dimensional material UV photodetectors.

Methods In this study, tapes are used to mechanically exfoliate $TlGaS_2$ single crystals into nanosheets, which are dry-transferred onto SiO_2/Si substrates using polydimethylsiloxane (PDMS). The structure and chemical composition of the nanosheets are determined via Raman spectroscopy and X-ray photoelectron spectroscopy (XPS). The morphology and thickness of the nanosheets are characterized using atomic force microscopy, and the spectral absorption range of the material is determined using an absorption spectrum test. The energy band structure and density of states of the $TlGaS_2$ material are calculated by first principles to determine its energy band structure, which uses density functional theory (DFT) theory with projector augmented-wave (PAW) pseudopotentials and a hybrid functional. The obtained $TlGaS_2$ nanosheets are fabricated into devices via a lift-off process using electron beam lithography and electron beam evaporation to obtain patterned two-terminal electrodes. The optoelectronic properties of the fabricated detector devices are tested using a semiconductor tester under laser irradiation or a mercury lamp with an added filter.

Results and Discussions According to the first-principle calculation [Fig. 2(a)], $TlGaS_2$ is an indirect bandgap semiconductor, and the valence band maximum is located at the Γ point. The bandgap width is 2.59 eV, and there is also a direct bandgap of 2.76 eV at the Γ point. The calculated results are consistent with the absorption spectrum test results for the material [Fig. 2(c)]. The $TlGaS_2$ nanosheets absorb energy near 480 nm (2.6 eV) through an indirect transition, and there is a transition from indirect to direct near 430 nm (4.85 eV), which shows a steep absorption edge. At the same time, the absorption spectra show that $TlGaS_2$ has high absorption in the UV region, even in the solar-blind UV region. The UV photodetector based on mechanically exfoliated $TlGaS_2$ nanosheets forms a good ohmic contact with the Ti/Au electrode. The photoelectric test (Fig. 3) shows that the detector's dark

current is on the order of 10^{-13} A. It has a certain response to optical signals smaller than 480 nm, and the steep increase in the photocurrent from 430 nm is consistent with the change trend of the absorption spectrum of the material. The detector exhibits an obvious photoresponse in the entire UV band. The best performance is achieved at 360 nm, with a responsivity of 57 mA/W and a detection rate of 2.69×10^{10} cm·Hz$^{1/2}$·W^{-1}. A transient test shows that the detector has a relatively fast response speed. After testing [Fig. 4(a)], the $TlGaS_2$ detector shows the on-state response time of 51.8 μs and the off-state response time of 45.1 μs. In addition, the detector exhibits a good low-frequency noise performance [Fig. 4(b)] and air stability [Fig. 4(c)]. Finally, a photocurrent-mapping test reveals the working principle of the detector. The material is excited by UV light to separate electrons and holes. They are affected by the potential difference between the two ends of the detector and move to both ends of the electrode to form the photocurrent, thus realizing conversion from an optical signal to an electrical signal.

Conclusions In this study, the crystal structure and chemical composition of mechanically exfoliated $TlGaS_2$ nanosheets are examined, and Tl and Ga are found to exist in the form of +1 and +3 valences, respectively. The energy band structure and density of states of $TlGaS_2$ are calculated using DFT, and the calculated bandgap value is almost consistent with the optical bandgap measured by the absorption spectrum experiment. Meanwhile, the absorption spectrum test shows that the $TlGaS_2$ material has high absorption in UV, even solar-blind UV, and a transition occurs from indirect bandgap to direct bandgap at 440 nm. Photodetectors based on $TlGaS_2$ nanosheets are successfully fabricated, and the working principle is that the photogenerated carriers generated by the photoconductive effect form the photocurrent under an external electric field. The working wavelength range of the detector is consistent with that of the absorption spectrum, which is less than 480 nm. In particular, for UV and solar-blind UV signals, the detector exhibits a distinct response. The detector has the best responsivity and detection rate under the 360 nm signal, and at the same time shows the very low dark current ($\sim10^{-13}$ A) and the very fast response time (51.8 μs for on-state and 45.1 μs for off-state), which is better than most wide-bandgap 2D material photodetectors. This work provides a new material choice for studying high response speed two-dimensional material UV photodetectors or for suppressing the dark current of the detectors.

Key words detectors; photodetector; ultraviolet light; $TlGaS_2$ nanosheets; fast response